Electronic structure of $KCa_2Nb_3O_{10}$ as envisaged by density functional theory and valence electron energy loss spectroscopy

Kulpreet Singh Virdi,[1,*] Yaron Kauffmann,[2] Christian Ziegler,[1,3] Pirmin Ganter,[1] Bettina V. Lotsch,[1,3] Wayne D. Kaplan,[2] Peter Blaha,[4] and Christina Scheu[1]

[1]*Department of Chemistry, Ludwig-Maximilians-Universität München, Butenandtstraße 11, Munich 81377, Germany*
[2]*Department of Materials Science and Engineering, Technion—Israel Institute of Technology, Haifa 32000, Israel*
[3]*Max Planck Institute for Solid State Research, Heisenbergstraße 1, Stuttgart 70569, Germany*
[4]*Institute of Materials Chemistry, Vienna University of Technology, Getreidemarkt 9/165-TC, A-1060 Vienna, Austria*

(Received 28 August 2012; revised manuscript received 22 January 2013; published 7 March 2013)

$KCa_2Nb_3O_{10}$ is a layered Dion–Jacobson-type perovskite important for a number of applications such as photocatalysis and as a building block for heteronanostructures. Despite this, some of its central electronic properties such as the band gap and dielectric function are not well understood. In this report we have attempted to determine the band gap and understand the electronic structure of $KCa_2Nb_3O_{10}$ using density functional theory. Simultaneously, the band gap and loss function have been determined experimentally using valence electron energy loss spectroscopy. The theoretical results indicate that $KCa_2Nb_3O_{10}$ is a direct band gap semiconductor with a sparse density of states close to the onset of the conduction band. The calculated band gap value of 3.1 eV is in excellent agreement with the 3.2 ± 0.1 eV measured experimentally. The loss functions computed and experimentally determined show good agreement up to 20 eV, but the theoretical peak positions at higher energy do not agree with the experimental electron energy loss spectrum. These transitions originate from K-3p, Ca-3p, and Nb-4p semicore states and their positions are not well described by Kohn-Sham eigenvalues. After a scissors shift of transitions due to these states by about 2.5 eV to higher energies we obtain good agreement with the experimental loss function and can thus explain the origin of all the features seen in the experimental electron energy loss spectrum.

DOI: 10.1103/PhysRevB.87.115108 PACS number(s): 77.22.Ch, 71.20.−b, 71.15.Mb, 79.20.Uv

I. INTRODUCTION

Since first being synthesized nearly three decades ago[1,2] $KCa_2Nb_3O_{10}$, a Dion–Jacobson-type perovskite, has constantly attracted the attention of the scientific community for various possibilities it offers. Researchers have reported it to be an interesting material for applications such as ionic conductivity[3] and photocatalysis.[4] Upon intercalation with Li, $KCa_2Nb_3O_{10}$ has been shown to turn superconducting.[5] Upon doping with Eu^{3+} or La^{3+} it has been reported to become photoluminescent.[6] In recent years interest in the material has surged again as it has been used as the parent compound for exfoliation into two-dimensional nanosheets, whereby the K^+ ions of the $KCa_2Nb_3O_{10}$ have been chemically replaced during exfoliation by bulky organic cations.[7] Possible applications of such nanosheets range from dielectrics to building blocks for layered heterostructures.[8,9] Despite the large interest in pure and doped $KCa_2Nb_3O_{10}$, a basic understanding of the electronic structure of this material is lacking. The crystal structure of $KCa_2Nb_3O_{10}$ was studied using single crystal x-ray diffraction analysis by Fukuoka *et al.*[10] whereby it was suggested to be orthorhombic, space group *Cmcm*. However, in this experiment only an average structural model could be obtained with partial occupation of some O sites.[10] Tokumitsu *et al.* argued[11] that as neutron beams interact more strongly with the nuclei than the x-rays, neutron diffraction offered the opportunity to better understand the positions of oxygen atoms. They improved[11] upon the structure model of Fukuoka *et al.*[10] and indicated a monoclinic structure (space group $P2_1/m$) with no partial occupancies.

Density functional theory (DFT) has proven to be an invaluable tool for understanding many material properties like bulk moduli, phase diagrams, and crystal structures;[12,13] however, its ability to successfully predict properties relating to excited states (band gaps in particular) has been less successful.[14,15] This is a direct consequence of the fact that the Hohenberg-Kohn theorem[16] is mathematically valid only for ground states.[17] Standard DFT has been infamous in the study of semiconductors for underestimating band gaps and more sophisticated, computationally expensive methods must be used. Recently, progress has been made for calculating band gaps more effectively by using the Tran-Blaha modified Becke Johnson (TB-mBJ) potential.[18] This approach has been successfully demonstrated[18] to predict band gaps of semiconductors (Si, Ge, GaAs, etc.), insulators (LiF, Ne, Kr, etc.), and even correlated transition metal oxides (MnO, NiO). Employing this approach[18] we have attempted to understand the electronic structure of $KCa_2Nb_3O_{10}$ by obtaining the band structure, density of states (DOS), dielectric function, and loss function.

With the advent of commercially available monochromators on transmission electron microscopes (TEM), determination of band gaps using valence electron energy loss spectroscopy (VEELS) has become an interesting experimental option,[19–22] specifically relating to nanostructures where other methods cannot offer sufficient spatial resolution.[23] In this work we have determined the band gap of $KCa_2Nb_3O_{10}$ using VEELS. In addition, the loss function S is determined from VEELS and subsequently compared to the theoretically calculated loss function.

 ©2013 American Physical Society

II. COMPUTATIONAL AND EXPERIMENTAL METHODOLOGY

A. Computational details

As an input, the structure of $KCa_2Nb_3O_{10}$ proposed by Tokumitsu *et al.*,[11] determined by powder neutron diffraction, was used for calculations as it offered well defined and fully occupied oxygen sites in contrast to the model of Fukuoka *et al.*[10] In this structure model[11] $KCa_2Nb_3O_{10}$ crystallizes into a monoclinic crystal, space group $P2_1/m$ (space group number 11). We have interchanged the crystal axes compared to Ref. 11 by redefining crystal parameters a, b, c, and γ to 14.859 Å, 7.7418 Å, 7.7073 Å, and 97.51°, respectively. Density functional theory based calculations were performed on $KCa_2Nb_3O_{10}$ using an augmented plane wave + local orbitals (APW + lo) approach as incorporated in the WIEN2K code.[24] The atomic spheres used for K, Ca, Nb, and O were 2.42, 2.03, 1.69, and 1.50 a.u. respectively. The wave functions in the atomic spheres were expanded as spherical harmonics up to angular momentum $l = 10$. Local orbitals were used for the semicore states (Ca-3s,3p; K-3s,3p; Nb-4s,4p; O-2s). In the interstitial region between the atomic spheres, a plane wave expansion was used, fixing the parameter $R_{MT}K_{\max} = 7$, which is the product of the smallest muffin tin radius and the largest plane wave $K_{\max}$. The adequacy of the choice of the plane wave basis set size was checked by additional calculations using $R_{MT}K_{\max} = 8$. The calculated forces on the atoms with this enlarged $R_{MT}K_{\max}$ stayed within the convergence criterion used for structure optimization, thereby validating the choice of the size of the plane wave basis set. For optimizing the atomic positions in the unit cell and determining the energy of the system, exchange correlation effects were treated using the generalized gradient approximation as proposed by Perdew, Burke, and Ernzerhof (PBE-GGA).[25]

Since it is well known that PBE-GGA underestimates band gaps,[26] the electronic structure calculations (DOS, band structure, and dielectric function) were performed using the TB-mBJ potential[18] which usually predicts band gaps with higher accuracy. The original Becke-Johnson potential[27] is an approximation to the "exact-exchange" optimized effective potential in atoms. Tran and Blaha[18] have introduced a weighing factor for the two terms of this potential (the approximate Slater potential and the response part), which is determined from the average of $\nabla\rho/\rho$ (where ρ corresponds to the electron density) of the specific system under investigation. It has been shown in numerous applications[18,28–30] that the TB-mBJ methodolgy predicts band gaps in very good agreement with experiment and much more expansive Green's function based (GW) calculations.

The irreducible Brillouin zone was sampled with a [2 × 4 × 4] k-point mesh for the self-consistency cycle which was taken to be converged when the forces on the atoms fell below 1.0 mRy/a.u. For geometry optimization the structure was optimized by minimizing the forces on the atoms, keeping the overall unit cell parameters constant. The structure was assumed relaxed when the force components on individual atoms fell below 5.0 mRy/a.u. A denser k mesh with [4 × 8 × 8] k points was then used to sample the irreducible Brillouin zone to extract the density of states and the optical properties. Optical properties were determined by employing the OPTIC program[31] of the WIEN2K code, whereby momentum matrix elements were computed in an energy range of −5 to 5 Ry. Two different calculations were performed; in the first, no scissor operator was used because of the usage of TB-mBJ potential[18] which models the valence and conduction band states well. However, the TB-mBJ potential does not give correct energy positions of the semicore states (K-3s,3p; Ca-3s,3p; Nb-4p) and in order to determine the dielectric function at higher energies, the transitions due to these states were shifted to a higher energy by an amount $\Delta E = 2.5$ eV in the ε_2 calculated from the momentum transfer matrix elements.

B. Synthesis

$KCa_2Nb_3O_{10}$ synthesis was carried out in a way similar to the one performed by Jacobson and co-workers.[2] Commercially available K_2CO_3 (Merck, 99% purity), $CaCO_3$ (Grüssing GmbH Germany, 99% purity), and Nb_2O_5 (Alfa Aesar, 99.5% purity) in a stoichiometric ratio of 1.1:4:3 were thoroughly ground and mixed. A preheating step at 900 °C was undertaken before firing up the pelletized compound to 1200 °C for 60 h. The purity of the as-synthesized $KCa_2Nb_3O_{10}$ was checked by means of x-ray diffraction where all reflections obtained were characterized as those of $KCa_2Nb_3O_{10}$. For TEM analysis, the $KCa_2Nb_3O_{10}$ was suspended in ethanol, stirred, and drop coated onto lacy carbon coated copper TEM grids (Plano GmbH Germany), and allowed to dry in air.

C. VEELS measurements and data analysis

The $KCa_2Nb_3O_{10}$ TEM samples were investigated using a FEI Titan 80-300 scanning transmission electron microscope equipped with a field emission gun, a Wien-type monochromator, and a Gatan Tridiem 866 energy filter having a 2k CCD camera to obtain the VEEL spectra. A freely suspended particle of $KCa_2Nb_3O_{10}$ was chosen and checked for thickness by obtaining an electron energy loss spectroscopy (EELS) thickness map which suggested that the thickness of the particle investigated was about 0.3 times the inelastic mean-free-path length. The sample was oriented into a random orientation such that it was not in a zone axis for a high-symmetry plane. Measurements for band gap and loss function extraction were performed in scanning transmission electron microscopy (STEM) mode with a stationary spot using convergence and collection angles of 9.5 mrad each. A spectrometer dispersion of 0.02 eV/channel was used for acquiring the VEEL spectra. Additionally, to obtain the core loss excitations Ca $M_{2,3}$ and Nb $N_{2,3}$ EEL spectrum was acquired in TEM mode from a different region using parallel illumination, collection angle (governed by the objective lens aperture and the spectrometer entrance aperture in TEM mode[32]) of 9.5 mrad, and a dispersion of 0.2 eV/channel. The chosen collection angle resulted in a momentum transfer of ∼3 Å^{-1}, due to which the contribution of dipole-forbidden transitions[32–34] to the EELS signal was reduced.

The VEEL spectra of $KCa_2Nb_3O_{10}$ were acquired in a two-step process. In the first step, 50 spectra were acquired with acquisition times of 0.14 s each, such that the spectra spanned across the tail of the zero-loss peak (ZLP) on the

negative side up to the valence loss features of importance (−6 to +34 eV). Next, 50 spectra were acquired with an acquisition time of 1.12 s each, where the spectra spanned from the tail of the ZLP on the positive side of the energy loss until the features of interest (+1 to +41 eV). The spectra in the first set containing the complete ZLP were aligned to get the maximum overlap between all ZLPs and were then added, to get a single spectrum, using EELS tools routines[35] implemented in the commercially available software package Digital Micrograph (Gatan Inc., Pleasanton California). The 50 spectra in the second set were also added to get a single spectrum. These two spectra were calibrated in the following way. The maximum of the ZLP in the first spectrum was defined to be zero energy loss. Then the uncalibrated second spectrum containing the valence loss features with a better signal-to-noise ratio was superimposed on the first spectrum and then calibrated such that the positions of valence loss excitations in both spectra overlapped. The calibrated spectra were then spliced to form a single spectrum which was used for subsequent analyses. The energy resolution, as governed by the full width at half maximum of the ZLP, was 0.2 eV and was achieved for settings where the ZLP was not symmetric. Due to this, the method of subtracting the mirrored negative side of ZLP[19,22] was not used for removing the ZLP contribution from the spectra. Instead a power-law function was used to describe the tail of the ZLP as has been used by Erni and Browning[36] and then subtracted from the spectrum to obtain the loss function. However, we did not use a Lorentzian fit of the first derivate like Erni and Browning[36] to determine the conduction band onset.

III. RESULTS AND DISCUSSION

A. DFT calculations

The crystal structure of $KCa_2Nb_3O_{10}$ is shown in Fig. 1. It consists of two-dimensional (2D) planes containing K, Ca, or Nb atoms parallel to the crystallographic (100) plane. There are two different NbO_2 planes in the structure, one located between the KO_2 and CaO planes (Nb atoms referred to subsequently as Nb3 and Nb4), the other located in the crystallographic (200) plane between two CaO planes (Nb atoms referred to subsequently as Nb1 and Nb2). Geometry optimization of the $KCa_2Nb_3O_{10}$ structure changed the fractional atomic positions (see Table I) up to 0.03 Å (Ca3) as compared to the experimental structure proposed by Tokumitsu *et al.* The Nb1(2)-O octahedra are not significantly modified; the corresponding Nb-O distances change by less than 0.02 Å. Overall the $Nb1(2)O_2$ plane is less buckled. On the other hand the Nb3(4)-O octahedra rotate slightly and the Nb-O distances change up to 0.07 Å. This makes the Nb3-O and Nb4-O octahedra more similar. Partly due to these rotations, but in particular due to large movements of the Ca ions, some Ca-O bond lengths change by up to 0.3 Å, thereby increasing the shortest Ca-O distances and making the complex Ca-O polyhedra more isotropic. The large changes around Ca also change the bond valence sums from 2.44–1.90–1.65–2.34 to 2.33–2.16–1.81–2.02 (Ca1–Ca2–Ca3–Ca4), making them much closer to the formal valence of Ca. Some K-O distances change by up to 0.2 Å which makes the K1–O2–K2 distances much more similar.

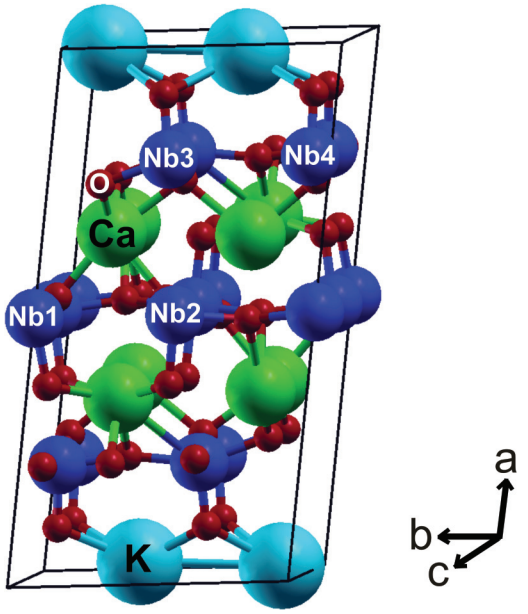

FIG. 1. (Color online) Unit cell of $KCa_2Nb_3O_{10}$ indicating the planes of K, Ca, and Nb atoms; Nb atoms in the median plane have been labeled Nb1 and Nb2 whereas the ones in the planes between K and Ca planes are labeled as Nb3 and Nb4.

The total density of states obtained using modified Becke-Johnson potential[18] showed the valence band having a width of about 5 eV separated from the conduction band by a band gap value of 3.1 eV (Fig. 2). At the conduction band onset the DOS is fairly low up to 4.3 eV, after which there is a sudden increase up to 6 eV, where another gap separates the conduction bands into two regions. The low-energy part of the DOS can be attributed to the semicore states as follows: Between −30.9 and −30.3 eV are the Nb-4p states (which incidentally are spin-orbit split by about 0.2 eV); between −28.6 and −27.9 eV K-3s states; between −20.2 and −19.0 eV Ca-3p states; between −18.4 and −16.2 eV O-2s states; between −11.3 and −10.8 eV K-3p states. Transitions from these semicore states into the conduction band should be delineated in the imaginary part of the dielectric function ε_2.

As is evident from the partial DOS (PDOS), the valence band is dominated by O-2p states with some admixture of Nb-d states, while in the conduction band Nb-d states dominate and the O-p PDOS is small (Fig. 2). We determined the contributions of t_{2g}- and e_g-like Nb orbitals to the conduction band. For this purpose a local coordinate system around each Nb site was introduced such that the axes point as close as possible towards the six O neighbors which form distorted octahedra around the Nb sites. In these local coordinate systems we call the two Nb-4d orbitals pointing towards the O atoms as e_g-like and the other three Nb-4d orbitals pointing between O atoms as t_{2g}-like. Of course the e_g-like and t_{2g}-like are no irreducible representations for this low-symmetry-point group. The partial DOS due to these Nb t_{2g}-like and e_g-like orbitals are shown in Fig. 3. We see that up to 6 eV the conduction band has a predominant t_{2g}-like character while the e_g-like orbitals dominate the partial DOS at higher energies.

TABLE I. Theoretically optimized (top row) and experimental (bottom row) atomic positions in $KCa_2Nb_3O_{10}$.

Ca 1	0.6495	0.7855	0.75
	0.653	0.78	0.75
Ca 2	0.3405	0.7023	0.75
	0.346	0.717	0.75
Ca 3	0.6384	0.2893	0.75
	0.628	0.322	0.75
Ca 4	0.3480	0.1969	0.75
	0.351	0.201	0.75
K 1	0.0203	0.6302	0.25
	0.035	0.616	0.25
K 2	0.0071	0.1226	0.25
	0.008	0.132	0.25
Nb 1	0.5	0	0
	0.5	0	0
Nb 2	0.5	0.5	0
	0.5	0.5	0
Nb 3	0.7900	0.5778	0.9960
	0.7848	0.571	0.004
Nb 4	0.7889	0.0733	0.9943
	0.789	0.075	0.987
O 1	0.6293	0.4998	0.0304
	0.629	0.495	0.033
O 2	0.9091	0.6220	0.9644
	0.905	0.594	0.983
O 3	0.7741	0.3211	0.0136
	0.77	0.316	0.012
O 4	0.7444	0.5503	0.75
	0.749	0.541	0.75
O 5	0.7764	0.5923	0.25
	0.775	0.574	0.25
O 6	0.5226	0.5660	0.75
	0.514	0.576	0.75
O 7	0.5131	0.7536	0.0673
	0.520	0.755	0.053
O 8	0.6286	0.0635	0.0486
	0.630	0.006	0.052
O 9	0.9067	0.0879	0.9530
	0.906	0.081	0.953
O 10	0.7464	0.8139	0.9869
	0.748	0.818	0.974
O 11	0.7389	0.0757	0.75
	0.733	0.065	0.75
O 12	0.7842	0.0504	0.25
	0.782	0.069	0.25
O 13	0.5309	0.9570	0.75
	0.528	0.973	0.75

As mentioned before, the four inequivalent Nb sites group into two different types (Nb1 and Nb2 in the central layer between two Ca layers and Nb3 and Nb4 between a K and Ca layer). The Nb DOS within such pairs is nearly the same, but the partial DOS from the different planes differ significantly (Fig. 4). Interestingly the conduction band onset at 3.1 eV is primarily due to Nb1 and Nb2 states, while Nb3 and Nb4 states are shifted to slightly higher energies. The unoccupied Ca-3*d* states are about 8–10 eV above the Fermi energy and coincide with the Nb-e_g states, while the K-3*d* states are shifted even higher up to 12–14 eV.

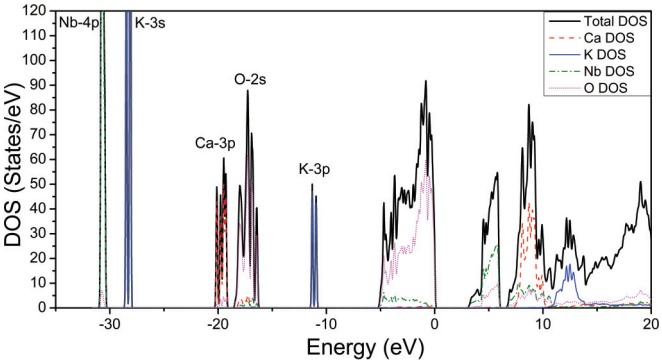

FIG. 2. (Color online) Calculated total (full black line) DOS of $KCa_2Nb_3O_{10}$ showing a band gap of 3.1 eV and sparse availability of conduction band states close to the onset of the conduction band. The partial DOS of Ca (red dashed line), K (blue full line), Nb (green dash-dot curve) and O (magenta dotted curve) show the respective partial contributions to the DOS.

The band structure of $KCa_2Nb_3O_{10}$ is shown in Fig. 5. One observes a large number of fairly flat bands at the top of the valence band (within 2 eV from the valence band maximum), while for the lower valence bands some dispersion is evident. Specifically, the top of the valence band is nearly degenerate at several high-symmetry points in *k* space (Γ, A, B, and C). On the contrary the conduction band onset at 3.1 eV is constituted by two strongly dispersive bands whose energy minima occur at the Γ and A points, thereby showing that $KCa_2Nb_3O_{10}$ is a direct band gap semiconductor. The conduction band states in the energy range 3.1–4.4 eV are quite dispersed, while bands in the energy range of 5.5–6.0 eV are less dispersed. As expected from the short Γ-A direction (large periodicity in direct space) and the 2D nature of $KCa_2Nb_3O_{10}$ where

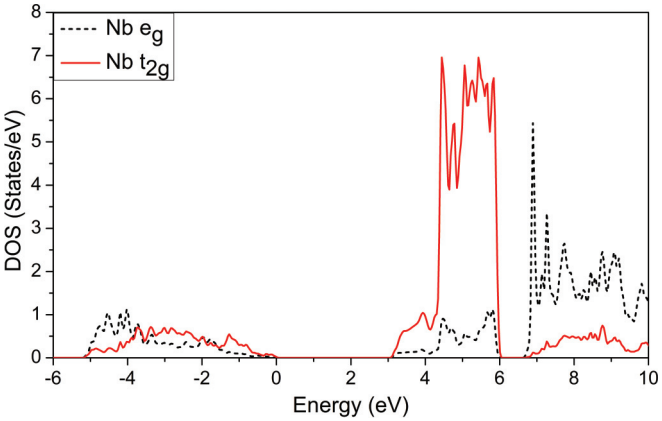

FIG. 3. (Color online) Partial DOS contribution of the e_g-like (dashed black curve) and t_{2g}-like (full red line) orbitals of Nb to the conduction and valence bands.

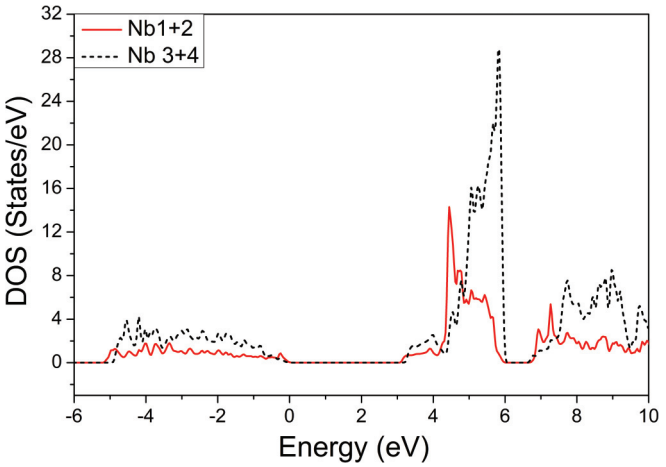

FIG. 4. (Color online) The partial DOS contribution shows two distinct varieties of Nb atoms, Nb1 and Nb2 (full red line) and Nb3 and Nb4 (dashed black curve) with the conduction band onset contributed by the Nb1, Nb2 atoms.

the Nb-O perovskitelike layers (with fairly localized wave functions) are completely decoupled in the a direction by the K layers, all bands in this direction are very flat.

The optical properties, namely the real and imaginary parts of the dielectric function ε and the loss function, were computed by the OPTIC program.[31] All these properties are in principle tensors of the order 3×3; however, simplifications were made for easier interpretation. While in monoclinic systems, the dielectric tensor contains nonzero off-diagonal elements,[31,37] we have neglected such (small) terms in our analysis. In addition the average dielectric function ε was defined as the average of the three diagonal elements ε_{xx}, ε_{yy}, ε_{zz} [Eq. (1)] for simplicity.

$$\varepsilon = (\varepsilon_{xx} + \varepsilon_{yy} + \varepsilon_{zz})/3. \quad (1)$$

The dielectric function is a complex function ($\varepsilon = \varepsilon_1 + \iota\varepsilon_2$) and its imaginary part ε_2 is obtained[31] from the joint density of states including the momentum matrix elements p between

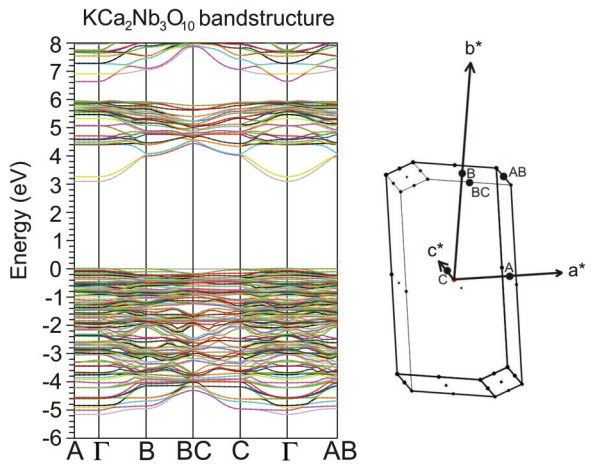

FIG. 5. (Color online) Band structure of $KCa_2Nb_3O_{10}$ (along with the shape of the Brillouin zone) indicating it to be a direct band gap semiconductor.

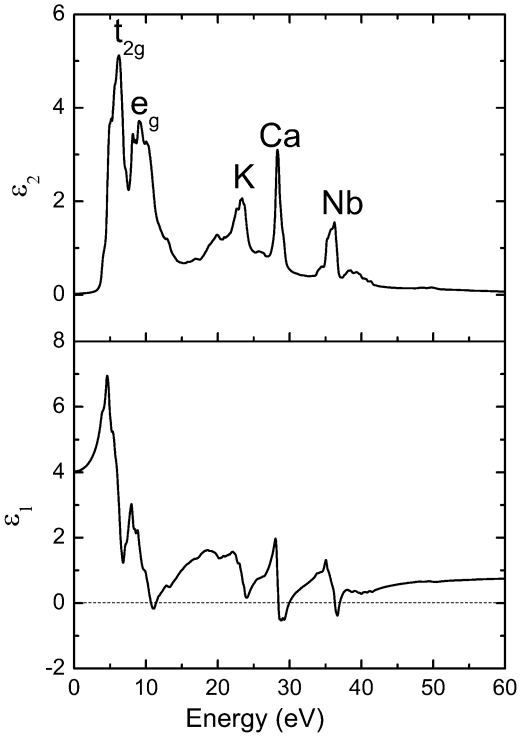

FIG. 6. Computed real and imaginary parts of the dielectric function of $KCa_2Nb_3O_{10}$. From the real part one would establish 11.3, 30.0, and 37.0 eV to be plasmon excitations.

occupied and empty states Eq. (2).

$$\varepsilon_{ij} \approx \frac{1}{\omega^2} \sum_{o,e} \int_k p_{i;o,e,k} p_{j;o,e,k} \delta(E_{e,k} - E_{o,k} - \omega). \quad (2)$$

The real part ε_1 has been extracted using the Kramers-Kronig transformation.[38] In addition, the loss function S, which is related to dielectric function[32] as described by Eq. (3), has also been calculated.

$$S = \mathrm{Im}\left[-\frac{1}{\varepsilon}\right] = \frac{\varepsilon_2}{\left(\varepsilon_1^2 + \varepsilon_2^2\right)}. \quad (3)$$

The average dielectric function is shown in Fig. 6. From the complex dielectric function the refractive index and the extinction coefficient could be extracted.[39] In addition from the real part, one could ascertain the position of plasmon excitation E_p as points where $\varepsilon_1(E)$ is zero and has a positive slope with respect to energy.[39–41] At three values of energy (11.3, 30.0, and 37.0 eV) these two conditions are satisfied, indicating plasmon excitation of valence electrons at these energy values. It is worth noting that close to $E = 24$ eV the value of ε_1 comes very close to zero but still does not cross the energy axis. From the real part of the dielectric function we have determined the ion clamped (high frequency) macroscopic dielectric constant ε^{∞} of $KCa_2Nb_3O_{10}$ as 0.77.[38]

It is worth mentioning that Li and co-workers[42] have determined the dielectric constant of $KCa_2Nb_3O_{10}$ in the low-frequency regime (10^1–10^6 Hz) to be varying between 500 and 1800. A comparison of our calculated dielectric function to their measurements would rather be inappropriate, because electronic transitions calculated in our methodology

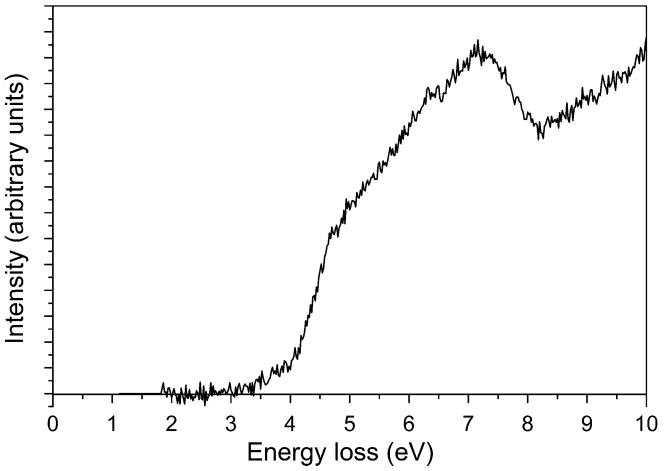

FIG. 7. Onset of the conduction band at 3.2 ± 0.1 eV indicated by ZLP subtracted VEEL spectrum of $KCa_2Nb_3O_{10}$.

constitute the predominant dielectric response only at very high frequencies (10^{13} Hz and higher).[39]

The imaginary part of the dielectric function offers insight into the interband transitions. A closer look at the partial density of states and the character of the corresponding bands enables us to analyze the features observed in ε_2. The initial set of transitions occurring between 4.5 and 7.0 eV is due to transitions from the valence band into the Nb-t_{2g} bands, whereas the one between 7.0 and 11.0 eV is due to excitations of valence electrons into the Nb-e_g states. The transitions depicted close to 25 eV are due to excitations from the K-3p bands into the K-3d states (located more than 12 eV above the valence band maximum), while the sharp peak around 28 eV corresponds to the promotion of electrons from Ca-3p states to the Ca-3d states in the upper conduction bands. Finally Nb-4p semicore electrons constitute the transitions starting at 35 eV.

B. VEELS and band gap extraction

VEEL spectrum of $KCa_2Nb_3O_{10}$ in the energy loss range 0–10 eV is shown in Fig. 7. One can establish that the onset of the conduction band is 3.2 ± 0.1 eV which confirms our calculated value of 3.1 eV and the value of 3.35 eV experimentally determined[4] by Domen and co-workers. The error in our measurement is governed by the calibration method and the signal-to-noise ratio. Improving the quality of data with regard to the onset of the conduction band is difficult. On one hand, one could improve the signal-to-noise ratio by increasing the exposure time, but then one risks increasing the chances of contamination, beam damage, and detector damage, which are common limitations in STEM and VEELS. Another possible alternative is choosing a thicker region for investigations, thereby increasing the scattering cross section. However, the chances of Cerenkov radiation causing an artifact for band gap extraction in the VEEL spectra increase for thicker samples.[19] Rafferty and Brown[43] proposed that for direct band gap semiconductors in the VEEL spectrum, the region close to the band onset could be described by $(E - E_g)^{0.5}$, where E_g is the band gap. Knowing from our calculations that $KCa_2Nb_3O_{10}$ is a direct band gap semiconductor, we avoid fitting such a function to the onset. Clearly a function of the form $(E - E_g)^{0.5}$ would indicate an abrupt onset; however, we observe a very gentle onset. The very gentle onset observed by us conforms well to the fact that only a few conduction band states are available below 4 eV.

It is necessary to highlight that we have not applied deconvolution to the acquired VEELS for removal of multiple scattering, a method which has been used regularly.[44–46] The justification lies in the fact that we have acquired VEEL spectra from a thin region (thickness ~0.3 mean-free-path length) in which the scattering cross section for multiple scattering events is negligible.

The surface plasmon is an important loss mechanism, for thin samples when probed in the transmission electron microscope, especially in the valence loss region. It has been suggested that for thin samples[44] this excitation can superimpose on other valence excitation, thereby making it hard to extract the band gap. Therefore it is necessary to understand if such an excitation is interfering in our measurements. The surface plasmon becomes an important loss mechanism only in cases where the thickness of the material is less than 20 nm (Ref. 32) or when the loss spectrum is acquired in aloof conditions (i.e., the beam is placed just outside the edge of the sample).[47] From EELS thickness maps we have estimated the thickness of the region investigated to be around 0.3 times the inelastic mean-free-path length. Using the model for calculating mean-free-path length proposed by Malis and co-workers[48] we estimate the thickness of our material to be about 42 nm. As such the chances for a surface plasmon signal making a significant contribution to the loss spectrum are negligible.

Cerenkov losses are another pitfall which can hinder[44] the identification of the conduction band onset from VEELS. When the velocity of an electron passing through a medium exceeds the phase velocity of light in that medium, Cerenkov radiation is generated.[19,32,49] Clearly, for electrons with an energy of 300 keV Cerenkov radiation would be generated in $KCa_2Nb_3O_{10}$ whose ε_1 varies between 4 and 7 in the energy range 0–5 eV. As such it is necessary to discuss the possible chances of such losses interfering with our measurements.

It has been known[50,51] that Cerenkov radiation has an angular distribution such that most of the radiation is confined within an angular width of the order of 0.1 mrad. This implies that for a conventionally used collection angle of about a few milliradians, nearly all Cerenkov radiation generated would be collected for an on-axis spectrometer entrance aperture.[21] One way of limiting the contribution of Cerenkov radiation would be using a dedicated dark-field spectrometer entrance aperture (for details see Ref. 19); however, that was not possible using our apparatus.

Cerenkov radiation generation can, however, be strongly damped when the thickness of the material probed is less than about 100 nm.[19,51–54] Erni and Browning showed[54] that there are negligible Cerenkov losses for thickness below 100 nm in materials with normalized emission rate below 0.9. The normalized emission rate[54] for $KCa_2Nb_3O_{10}$ can be determined on the basis of the computed maximum value of ε_1 (6.95) to be 0.76. Therefore on the basis of the analysis of Erni and Browning,[54] it can be deduced that in a VEELS measurement from a 42-nm-thick region of $KCa_2Nb_3O_{10}$, the

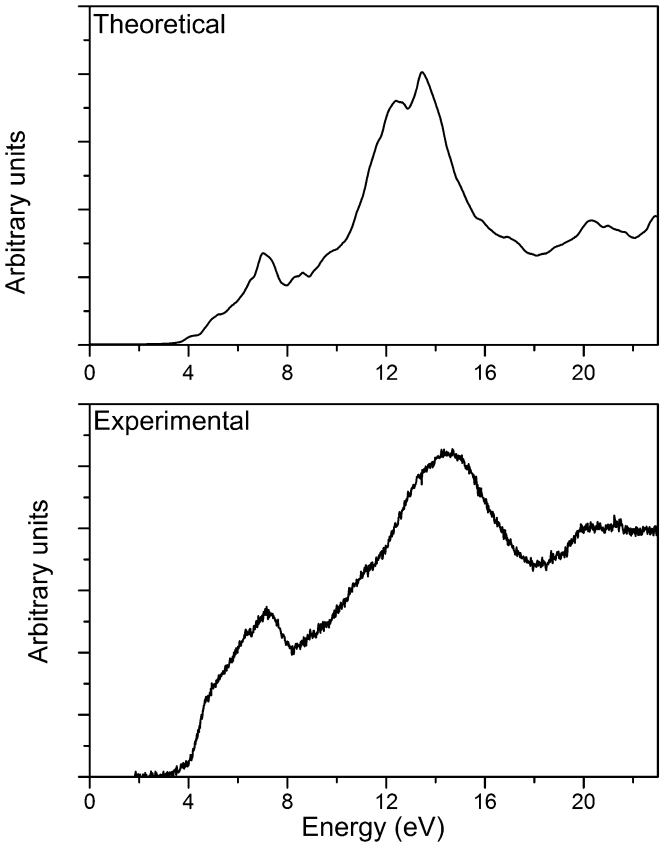

FIG. 8. Theoretically computed and experimentally determined loss functions.

Cerenkov radiation generation is heavily damped and as such does not contribute significantly to the scattering cross section.

van Benthem and co-workers determined[45] the optical properties of $SrTiO_3$ using VEELS (STEM mode, 6.5 mrad convergence and collection angles, respectively) and vacuum ultraviolet spectroscopy. They found[45] good agreement between the two methods and concluded that Cerenkov losses did not contribute to the VEELS signal in any significant manner.

In light of these results[19,21,45,50–54] and the fact that our calculated and experimentally determined loss function show good agreement (Fig. 8), it can be assumed that Cerenkov losses on account of damping do not contribute significantly to the VEEL spectra acquired.

The band gap values determined using VEELS (3.2 ± 0.1 eV) and DFT (3.1 eV) compare well with the band gap value of 3.35 eV measured by Domen and co-workers[4] using photocatalysis. This shows the success in usage of VEELS and modified Becke-Johnson potentials[18] for ascertaining the band gaps with reasonable accuracy.

C. Loss function comparison

In an electron energy loss spectrum, the double differential scattering cross section[32] is directly proportional to the loss function S. Therefore the intensity measured in EELS experiments is directly related to the loss function. A big advantage of this technique is the easy identification of plasmon excitations,[39] which in thicker samples would dominate the EELS. Moreover it serves as a good method of comparing the agreement between theory and experiments. To this end the loss function of $KCa_2Nb_3O_{10}$ was extracted from experimental VEELS and theoretically computed dielectric function and plotted for comparison in Fig. 8. When one compares the experimental and calculated loss functions one sees good agreement in the regime $E < 20$ eV.

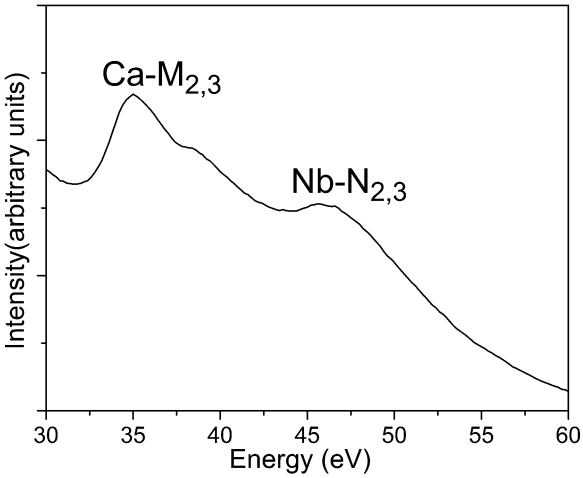

FIG. 9. EEL spectrum acquired in TEM mode indicating Ca $M_{2,3}$ and Nb $N_{2,3}$ edges.

D. Loss function at higher energies

In order to better understand the semicore states, we acquired EELS in TEM mode with a larger dispersion (0.2 eV/channel). The EEL spectrum is shown in Fig. 9. There are two distinct features visible, namely the peaks at 35 and 45.5 eV. A comparison with the literature[55,56] helps in identifying the feature with a maximum at 35 eV to be the Ca $M_{2,3}$ edge. Bach and co-workers have shown[57] that Nb in an oxidation state of $+5$ yields a Nb $N_{2,3}$ edge at 46 eV; hence we designate the peak at 45.5 eV as that due to Nb $N_{2,3}$ excitation.

In the calculated imaginary part of the dielectric function, shown in Fig. 6, we had designated the transitions at 28 and 37 eV to electrons from the Ca-3p and Nb-4p states. The excitations due to the corresponding energy levels (Ca-3p and Nb-4p) in EEL spectrum occur at higher energies (35 eV Ca $M_{2,3}$ edge and 46 eV Nb $N_{2,3}$ edge). Even taking into account that peaks in loss function are usually a few eV higher in energy than the peaks in ε_2, because low values (zeroes) in ε_1 appear usually a few eV after peaks in ε_2, the positions of excitations due to Ca-3p and Nb-4p electrons are not optimal. This points to shortcomings in our computational methodology specifically for semicore states. It has been shown previously[58] that DFT based methods predict the semicore states at higher energies than the ones that are experimentally measured. This is related to the fact that these methods cancel the self-interaction incompletely,[59] and also the TB-mBJ method cannot cure the problems for these low-lying states. In addition, such localized excitations are known[60] to produce large excitonic effects which cannot be modeled by single particle approaches.

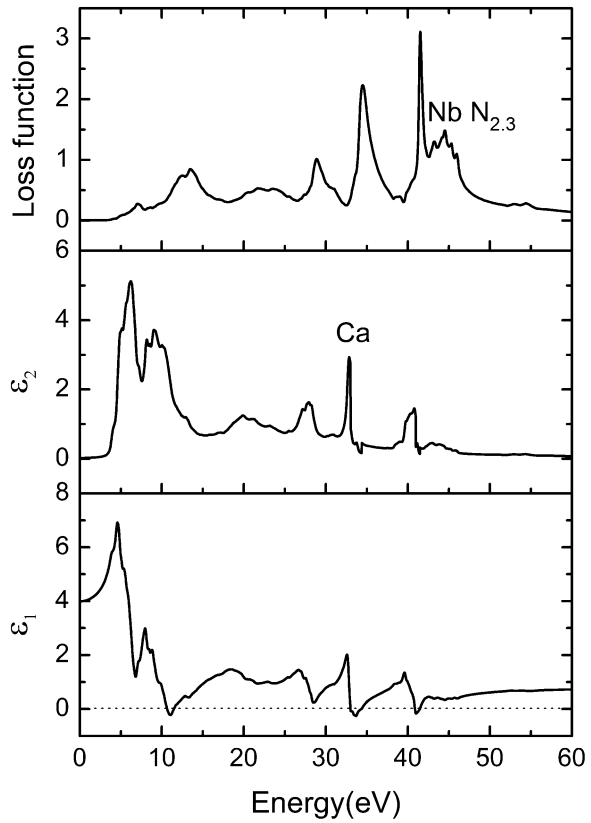

FIG. 10. The corrected dielectric function and loss function obtained by shifting the transitions due to semicore states by 2.5 eV towards higher energies.

In order to model the high energy loss function in a more realistic manner, we computed ε_2 due to valence and semicore states separately. The momentum transfer matrix was computed, first using all the electrons and then using only the valence band electrons ($E > -5.3$ eV). Then the ε_2 calculated for valence band electrons was subtracted from the ε_2 calculated for all electrons to get ε_2 for the semicore states. This ε_2 due to the semicore electrons was shifted by energy ΔE where $\Delta E > 0$ because the semicore states are located at energies lower than what were computed. Then the partial ε_2 due to the valence electrons and the semicore states after the shift were added to get the corrected ε_2. Then the Kramers-Kronig analysis was applied on this corrected ε_2 to get the real part of the dielectric function and the loss function. This procedure was undertaken for different values of ΔE until a good agreement was reached between the theoretical and experimental loss functions with regard to the positions of Ca $M_{2,3}$ and Nb $N_{2,3}$ edges. We found the best agreement using a ΔE value of 2.5 eV. The calculated ε_1, ε_2, and loss function, after correction, are shown in Fig. 10. In the corrected loss function, the feature at 29 eV stems from the excitation of K-3p electrons, the peak around 34 eV from Ca-3p electrons, and the broad Nb-$N_{2,3}$ edge is between 40 and 47 eV. These energies agree well with the experimental EEL spectrum (Fig. 9).

IV. CONCLUSIONS

Density functional theory based calculations show that the $KCa_2Nb_3O_{10}$ structure is more symmetric than the experimental structure previously proposed and some bond distances (in particular Ca-O) differ by as much as 0.3 Å. The central NbO_2 plane is less buckled. $KCa_2Nb_3O_{10}$ is a direct band gap semiconductor with a calculated band gap of 3.1 eV. The conduction band onset is dominated by Nb1, Nb2 t_{2g}-like states (in the central plane between two Ca layers), whereas the Nb3, Nb4 (between K and Ca layers) states are shifted upwards. The large crystal field separates the empty Nb t_{2g} and e_g states by a small gap. On the other hand the valence band is dominated by O-2p states. The Ca-3d (and even more the K-3d) states start only at more than 8 eV above the valence band maximum. The band gap value of 3.2 ± 0.1 eV extracted from the STEM-VEELS measurement matches well with the theoretical results and a value reported in the literature. The loss function shows good agreement between theory and experiment up to about 20 eV but large deviations occur at higher energies. This comes about because the position of the semicore states predicted DFT calculations is higher than in reality, and for a proper modeling of the loss function at such high energies one needs to manually shift the position of the transitions due to these states.

ACKNOWLEDGMENTS

This work was partially supported through the financial endowment of the German Science Foundation through the cluster of excellence Nanosystems Initiative Munich (NIM) and the Center for Nanoscience (CeNS). K.S.V. is grateful to the Elite Network of Bavaria for financial support. P.B. was supported by the SFB-F41 (ViCoM) project of the Austrian Science Funds (FWF). We thank Professor Ray Egerton for fruitful discussions and insightful comments.

*Author for correspondence: kulpreet.virdi@cup.uni-muenchen.de

[1]M. Dion, M. Ganne, and M. Tournoux, Mater. Res. Bull. **16**, 1429 (1981).
[2]A. J. Jacobson, J. W. Johnson, and J. T. Lewandowski, Inorg. Chem. **24**, 3727 (1985).
[3]V. Thangadurai and W. Weppner, J. Mater. Chem. **11**, 636 (2001).
[4]K. Domen, J. Yoshimura, T. Sekine, A. Tanaka, and T. Onishi, Cat. Lett. **4**, 339 (1990).
[5]H. Fukuoka, T. Isami, and S. Yamanaka, Chem. Lett. **26**, 703 (1997).
[6]M. A. Bizeto, V. R. L. Constantino, and H. F. Brito, J. Alloys Compd. **311**, 159 (2000).
[7]Y. Ebina, T. Sasaki, and M. Watanabe, Solid State Ionics **151**, 177 (2002).
[8]M. Osada and T. Sasaki, Adv. Mater. **24**, 210 (2012).
[9]B. Li, M. Osada, T. C. Ozawa, Y. Ebina, K. Akatsuka, R. Ma, H. Funakubo, and T. Sasaki, ACS Nano **4**, 6673 (2010).
[10]H. Fukuoka, T. Isami, and S. Yamanaka, J. Solid State Chem. **151**, 40 (2000).

[11]T. Tokumitsu, K. Toda, T. Aoyagi, D. Sakuraba, K. Uematsu, and M. Sato, J. Ceram. Soc. Jpn. **114**, 795 (2006).
[12]E. Kaxiras, *Atomic and Electronic Structure of Solids* (Cambridge University Press, Cambridge, UK, 2003).
[13]J. Hafner, Acta Mater. **48**, 71 (2000).
[14]A. Seidl, A. Görling, P. Vogl, J. A. Majewski, and M. Levy, Phys. Rev. B **53**, 3764 (1996).
[15]W. Ku and A. G. Eguiluz, Phys. Rev. Lett. **89**, 126401 (2002).
[16]P. Hohenberg, and W. Kohn, Phys. Rev. **136**, B864 (1964).
[17]A. S. Bamzai and B. M. Deb, Rev. Mod. Phys. **53**, 95 (1981).
[18]F. Tran and P. Blaha, Phys. Rev. Lett. **102**, 226401 (2009).
[19]L. Gu, V. Srot, W. Sigle, C. Koch, P. van Aken, F. Scholz, S. B. Thapa, C. Kirchner, M. Jetter, and M. Rühle, Phys. Rev. B **75**, 195214 (2007).
[20]J. Park, S. Heo, J. Chung, H. Kim, H. Lee, K. Kim, and G. Park, Ultramicroscopy **109**, 1183 (2009).
[21]M. Stöger-Pollach, H. Franco, P. Schattschneider, S. Lazar, B. Schaffer, W. Grogger, and H. W. Zandbergen, Micron **37**, 396 (2006).
[22]S. Lazar, G. A. Botton, M.-Y. Wu, F. D. Tichelaar, and H. W. Zandbergen, Ultramicroscopy **96**, 535 (2003).
[23]T. Kuykendall, P. Ulrich, S. Aloni, and P. Yang, Nat. Mater. **6**, 951 (2007).
[24]P. Blaha, K. Schwarz, G. K. H. Madsen, D. Kvasnicka, and J. Luitz, WIEN2*k: An Augmented Plane Wave Plus Local Orbitals Program for Calculating Crystal Properties, User's Guide*, edited by K. Schwarz (Vienna University of Technology, Austria, 2001).
[25]J. P. Perdew, K. Burke, and M. Ernzerhof, Phys. Rev. Lett. **77**, 3865 (1996).
[26]J. Heyd, J. E. Peralta, G. E. Scuseria, and R. L. Martin, J. Chem. Phys. **123**, 174101 (2005).
[27]A. D. Becke and E. R. Johnson, J. Chem. Phys. **124**, 221101 (2006).
[28]D. J. Singh, S. S. A. Seo, and H. N. Lee, Phys. Rev. B **82**, 180103(R) (2010).
[29]W. Feng, D. Xiao, J. Ding, and Y. Yao, Phys. Rev. Lett. **106**, 016402 (2011).
[30]D. Koller, F. Tran, and P. Blaha, Phys. Rev. B **83**, 195134 (2011).
[31]C. Ambrosch-Draxl and J. O. Sofo, Comput. Phys. Commun. **175**, 1 (2006).
[32]R. F. Egerton, *Electron Energy-Loss Spectroscopy in the Electron Microscope* (Springer Science + Business Media, New York, 2011).
[33]J. M. Auerhammer and P. Rez, Phys. Rev. B **40**, 2024 (1989).
[34]H. Ma, S. H. Lin, R. W. Carpenter, and O. F. Sankey, J. Appl. Phys. **68**, 288 (1990).
[35]D. R. G. Mitchell and B. Schaffer, Ultramicroscopy **103**, 319 (2005).
[36]R. Erni and N. D. Browning, Ultramicroscopy **107**, 267 (2007).
[37]Y. Abraham, N. A. W. Holzwarth, and R. T. Williams, Phys. Rev. B **62**, 1733 (2000).
[38]H. Fröhlich, *Theory of Dielectrics* (Oxford University Press, Oxford, UK, 1958).
[39]M. Fox, *Optical Properties of Solids* (Oxford University Press, Oxford, UK, 2010).
[40]V. Gallegos-Orozco, R. Martínez-Sánchez, and F. Espinosa-Magaña, Phys. Rev. B **77**, 045128 (2008).
[41]V. J. Keast, A. J. Scott, M. J. Kappers, C. T. Foxon, and C. J. Humphreys, Phys. Rev. B **66**, 125319 (2002).
[42]B. Li, M. Osada, Y. Ebina, T. C. Ozawa, R. Ma, and T. Sasaki, Appl. Phys. Lett. **96**, 182903 (2010).
[43]B. Rafferty and L. M. Brown, Phys. Rev. B **58**, 10326 (1998).
[44]M. Stöger-Pollach, Micron **39**, 1092 (2008).
[45]K. van Benthem, C. Elsässer, and R. H. French, J. Appl. Phys. **90**, 6156 (2001).
[46]A. D. Dorneich, R. H. French, H. Müllejans, S. Loughin, and M. Rühle, J. Microsc. **191**, 286 (1998).
[47]M. R. S. Huang, R. Erni, H.-Y. Lin, R.-C. Wang, and C.-P. Liu, Phys. Rev. B **84**, 155203 (2011).
[48]T. Malis, S. C. Cheng, and R. F. Egerton, J. Electron Microsc. Tech. **8**, 193 (1988).
[49]F. J. García de Abajo, Rev. Mod. Phys. **82**, 209 (2010).
[50]C. von Festenberg, Z. Phys. **214**, 464 (1968).
[51]C. von Festenberg, Z. Phys. **227**, 453 (1969).
[52]E. Kröger, Z. Phys. **216**, 115 (1968).
[53]F. J. Garcia de Abajo, A. Rivacoba, N. Zabala, and N. Yamamoto, Phys. Rev. B **69**, 155420 (2004).
[54]R. Erni and N. D. Browning, Ultramicroscopy **108**, 84 (2008).
[55]K. S. Katti, M. Qian, D. W. Frech, and M. Sarikaya, Microsc. Microanal. **5**, 358 (1999).
[56]C. C. Ahn, O. L. Krivanek, R. P. Burgner, M. M. Disko, and P. R. Swann, *EELS Atlas* (HREM Facility, Arizona State University, Tempe, AZ, 1983).
[57]D. Bach, R. Schneider, D. Gerthsen, J. Verbeeck, and W. Sigle, Microsc. Microanal. **15**, 505 (2009).
[58]M. Arai, S. Kohiki, H. Yoshikawa, S. Fukushima, Y. Waseda, and M. Oku, Phys. Rev. B **65**, 085101 (2002).
[59]T. Miyake, P. Zhang, M. L. Cohen, and S. G. Louie, Phys. Rev. B **74**, 245213 (2006).
[60]R. Laskowski and P. Blaha, Phys. Rev. B **82**, 205104 (2010).